

A comparison of methods to balance geophysical flows

MANITA CHOUKSEY^{1,2,*}, CARSTEN EDEN², GÖKCE TUBA MASUR³, AND MARCEL OLIVER^{4,5}

¹Institut für Umweltphysik, Universität Bremen and MARUM, Germany

²Institut für Meereskunde, Universität Hamburg, Germany

³Institut für Atmosphäre und Umwelt, Goethe Universität Frankfurt, Germany

⁴Mathematical Institute for Machine Learning and Data Science,
KU Eichstätt–Ingolstadt, Germany

⁵Constructor University, Bremen, Germany

*Corresponding author: manita.chouksey@uni-bremen.de

Abstract

We compare a higher-order asymptotic construction for balance in geophysical flows with the method of “optimal balance”, a purely numerical approach to separate inertia-gravity waves from vortical modes. Both methods augment the linear geostrophic mode with dependent inertia-gravity wave mode contributions, the so-called slaved modes, such that the resulting approximately balanced states are characterized by very small residual wave emission during subsequent time evolution. In our benchmark setting – the single-layer rotating shallow water equations in the quasi-geostrophic regime – the performance of both methods is comparable across a range of Rossby numbers and for different initial conditions. Cross-balancing, i.e. balancing the model with one method and diagnosing the imbalance with the other, suggests that both methods find approximately the same balanced state. Our results also reinforce results from previous studies suggesting that spontaneous wave emission from balanced flow is very small.

We further compare two numerical implementations of each of the methods: one pseudospectral, and the other a finite difference scheme on the standard C-grid. We find that a state that is balanced relative to one numerical scheme is poorly balanced for the other, independent of the method that was used for balancing. This shows that the notion of balance in the discrete case is fundamentally tied to a particular scheme.

1 Introduction

Geophysical flows are characterized by rapid rotation of the frame of reference and by density stratification in the vertical. In the mid-latitudes, the dominant

37 force balance is between the Coriolis force due to rotation and the pressure
 38 gradient forces. The leading order concept, geostrophic balance, is exact in
 39 linearized dynamics; corrections beyond the leading order are more subtle, as
 40 nonlinear interactions begin to play a role. In practical terms, a well-balanced
 41 state is one that minimizes fast geostrophic adjustment by gravity wave activity
 42 in its subsequent time evolution.

43 The necessity to provide balanced initial conditions was recognized early
 44 in the development of numerical weather prediction (see, e.g., Lynch 2006 for
 45 a historical account). Machenhauer (1977) and Baer and Tribbia (1977) pio-
 46 neered the idea of *nonlinear normal mode initialization*, where Machenhauer
 47 obtained a first consistent nonlinear correction to a linear mode decomposition,
 48 which corresponds to the quasi-geostrophic balanced state (Leith, 1980). Baer
 49 and Tribbia, in the same year, proposed a multiple time-scale expansion which
 50 produces consistent higher order balance relations and gave explicit second or-
 51 der expressions. Warn et al. (1995) revisit the problem from a more abstract
 52 perspective, see Section 3.1 below. They reformulate the procedure without the
 53 need to introduce explicit fast-time and slow-time variables, and raise the issue
 54 that the resulting series is asymptotic, but not necessarily convergent.

55 Geometrically, a balance relation defines a *slow manifold*. A slow manifold
 56 is a submanifold of the phase space on which the solution trajectory evolves
 57 more slowly than anywhere else. For systems with a small asymptotic order
 58 parameter, “more slowly” is usually defined as “increases at a lower asymptotic
 59 rate as the order parameter goes to zero”. In the well-studied case of so-called
 60 normally hyperbolic systems – the van der Pol oscillator being a classical ex-
 61 ample – slow manifolds are attracting, unique, and exactly invariant. In this
 62 situation, it is possible to reduce the dynamics *exactly* to a dynamical system of
 63 lesser dimension on the slow manifold. Large scale geophysical fluid flow, on the
 64 other hand, is essentially inviscid. The Kolmogorov scale at which molecular
 65 viscosity becomes relevant is so far removed from the scales of interest that,
 66 for the purpose of characterizing balance, we need to work in the conceptual
 67 framework of Hamiltonian dynamics.

68 For Hamiltonian systems, existence of exactly invariant slow manifolds is
 69 too much to hope for. MacKay (2004), for example, constructs an elementary
 70 example which shows that an exactly invariant slow manifold cannot survive
 71 small generic Hamiltonian perturbations. He argues that a useful notion of
 72 slow manifold should include any submanifold of phase space with the following
 73 properties:

- 74 (i) The vector field is approximately tangent to the manifold, i.e., the mani-
 75 fold is nearly invariant,
- 76 (ii) The component of the vector field normal to the manifold grows strongly
 77 away from the manifold, i.e., the typical dynamic time scale off the man-
 78 ifold is much faster than the time rate of change on the manifold.

79 In this framework, slow manifolds are not unique. One slow manifold may be
 80 better than another in the sense that the approximate invariance of the manifold

81 under the flow is more accurate. Often, a hierarchy of slow manifolds is given
 82 by an asymptotic series. In this situation, nonexistence of an exactly invariant
 83 slow manifold is seen through the divergence of the asymptotic series. Yet,
 84 applying optimal truncation, exponential smallness of remainders can often be
 85 proved—see, e.g., Vanneste and Yavneh (2004) for exponential asymptotics of a
 86 simple model equation, Vanneste (2013) for a review from the geophysical fluid
 87 dynamics perspective, and MacKay (2004) and references therein for a more
 88 mathematical perspective.

89 For a practical decomposition of the state variables into their balanced and
 90 unbalanced components, an optimal truncation of the divergent series is not
 91 directly available. Therefore, high-accuracy diagnostics will either need to use
 92 a fixed, but possibly higher-order balance, or rely on a purely numerical proxy
 93 for optimal truncation, known as *optimal balance*. Regarding the first practical
 94 method, fixed higher-order asymptotics, Chouksey et al. (2018) have shown
 95 that, in order to diagnose the true gravity wave signal of waves emitted from
 96 an unstable jet, the residual of first order balance obtained from the nonlinear
 97 normal mode initialization procedure of Machenhauer (1977) is still dominated
 98 by slaved (slow) modes, not by the true wave signal, which only becomes visible
 99 at third or fourth order (Eden et al., 2019a), if at all. This is of relevance since
 100 wave emission is proposed as a significant sink of meso-scale eddy energy globally
 101 in the ocean from laboratory experiments (Williams et al., 2008) and idealized
 102 numerical simulations (Brüggemann and Eden, 2015; Sugimoto and Plougonven,
 103 2016), but it is possible that the signals discussed in those experiments are
 104 related to the so-called slaved modes and not to actual wave emission.

105 The second practical method for computing balance was pioneered by Viúdez
 106 and Dritschel (2004). Their *optimal potential vorticity balance* (OPV balance)
 107 was first conceived as a modification of a Lagrangian contour-advection numer-
 108 ical code in which the perturbation potential vorticity is slowly “ramped” from
 109 a trivial state to a fully nonlinear state “in which the amount of inertia-gravity
 110 waves is minimal”, but the original approach by Viúdez and Dritschel can be for-
 111 mulated for any model code as shown below. The approach is attractive because
 112 it produces high quality balance without any explicit asymptotics at non-trivial,
 113 but moderate computational expense, and is relatively easy to implement for a
 114 given numerical code.

115 Cotter (2013) realized that Viúdez and Dritschel’s procedure can be under-
 116 stood theoretically in terms of adiabatic invariance in the following sense: A
 117 trajectory that is initially close to a slow manifold, thus evolving approximately
 118 along this manifold, will continue to do so when the manifold is deformed slowly
 119 in time. Cotter provided proof, in the context of a finite-dimensional Hamilto-
 120 nian system, that the resulting balance is exponentially accurate, just as balance
 121 itself can only be defined up to exponentially small remainders. His argument
 122 presumes that the required integration is performed over an unbounded interval
 123 of time. Gottwald et al. (2017) studied optimal balance for the same finite-
 124 dimensional model restricted to a finite interval of time, which is necessary for
 125 any practical implementation. They realized that the required ramp function
 126 must satisfy consistency conditions at the temporal end points that preclude

127 the use of analytic normal form theory for the mathematical analysis. Yet,
 128 they were able to prove exponential estimates, albeit with a smaller power of
 129 the time separation parameter in the exponent. Thus, the state produced by
 130 “optimal balance” (here *not* “optimal *potential vorticity* balance” because the
 131 principle goes beyond a potential vorticity formulation of the problem) is not
 132 optimal in the strict sense, but very good in the sense that the remainder is
 133 small beyond all orders, and arguably the best *practically accessible* algorithm
 134 for flow separation.

135 In this study, we compare the higher-order balancing method by Warn et al.
 136 (1995) with the optimal balance method by Masur and Oliver (2020) using
 137 two different discretizations of the single layer shallow water equations, and for
 138 two qualitatively different initial states. In the following section, the model
 139 equations and their spectral representation are specified. Both methods are re-
 140 derived within the same framework in Section 3. It turns out that they can both
 141 be understood as a correction to the linear geostrophic mode \mathbf{z}_0 for the nonlin-
 142 ear model, using only \mathbf{z}_0 itself. In Section 4, the numerical codes, our model
 143 diagnosis strategy, and the initial conditions are detailed. Section 5 presents
 144 the results of the comparison. The paper concludes with a short discussion.

145 2 Model description

146 2.1 The single layer model

As a simple test case, we take a reduced gravity model for a single layer of
 constant density with mean height H_0 . The dimensional equations of motion
 for velocity \mathbf{u} and perturbation height h are given by

$$\partial_t \mathbf{u} + \mathbf{u} \cdot \nabla \mathbf{u} + f \mathbf{u}^\perp + g \nabla h = 0, \quad (1a)$$

$$\partial_t h + H_0 \nabla \cdot \mathbf{u} + \nabla \cdot (h \mathbf{u}) = 0, \quad (1b)$$

147 where \mathbf{u}^\perp denotes anticlockwise rotation of the vector $\mathbf{u} = (u, v)$ by $\pi/2$, i.e.
 148 $\mathbf{u}^\perp = (-v, u)$, f is the Coriolis parameter, and g the acceleration due to gravity.
 149 We non-dimensionalize (1) in terms of the usual Rossby (Ro), Burger (Bu), and
 150 Froude (Fr) numbers

$$\text{Ro} = \frac{U}{f_0 L}, \quad \text{Bu} = \frac{\text{Ro}^2}{\text{Fr}^2}, \quad \text{and} \quad \text{Fr} = \frac{U}{c} \quad (2)$$

where f_0 denotes the constant background rate of rotation and $c^2 = gH_0$ is the
 phase speed of gravity waves in the high wavenumber limit. U and L denote the
 horizontal velocity scale and length scale respectively. Assuming that Coriolis
 and pressure gradient forces approximately balance and choosing the *fast* time
 scale associated with the propagation of gravity waves, we have

$$\partial_t \mathbf{u} + f \mathbf{u}^\perp + \nabla h = -\text{Ro} \mathbf{u} \cdot \nabla \mathbf{u}, \quad (3a)$$

$$\partial_t h + \text{Bu} \nabla \cdot \mathbf{u} = -\text{Ro} \nabla \cdot (h \mathbf{u}), \quad (3b)$$

where all symbols refer to non-dimensional quantities. We now assume a constant rate of rotation, taking the scaled Coriolis parameter $f = 1$ and choose the quasi-geostrophic distinguished limit by setting $\text{Bu} = 1$.

2.2 Normal mode representation

We consider the model on a doubly periodic square domain of length 2π . Using the Fourier representation

$$\mathbf{u}(\mathbf{x}, t) = \sum_{\mathbf{k} \in \mathbb{Z}^2} \mathbf{u}_{\mathbf{k}}(t) e^{i\mathbf{k} \cdot \mathbf{x}} \quad (4)$$

where the complex coefficients satisfy $\mathbf{u}_{-\mathbf{k}} = \mathbf{u}_{\mathbf{k}}^*$ so that $\mathbf{u}(\mathbf{x}, t)$ is real, with a corresponding representation for h , writing $\mathbf{z}_{\mathbf{k}} = (u_{\mathbf{k}}, v_{\mathbf{k}}, h_{\mathbf{k}})$, and denoting the vector of all Fourier coefficients by $\mathbf{z} = (\mathbf{z}_{\mathbf{k}})_{\mathbf{k} \in \mathbb{Z}^2}$, we write (3) in the form

$$\frac{d\mathbf{z}}{dt} = i\mathbf{A}\mathbf{z} + \text{Ro} \mathbf{N}(\mathbf{z}, \mathbf{z}). \quad (5)$$

The system matrix \mathbf{A} is given by

$$\mathbf{A}_{\mathbf{k}} = \begin{pmatrix} 0 & -i & -k \\ i & 0 & -\ell \\ -\text{Bu} k & -\text{Bu} \ell & 0 \end{pmatrix}, \quad \mathbf{A} = (\mathbf{A}_{\mathbf{k}})_{\mathbf{k} \in \mathbb{Z}^2}, \quad \mathbf{k} = (k, \ell) \quad (6)$$

and the nonlinear interactions $\mathbf{N}(\mathbf{z}, \mathbf{z}) = (\mathbf{N}_{\mathbf{k}})_{\mathbf{k} \in \mathbb{Z}^2}$ are given by the symmetric bilinear form

$$\mathbf{N}_{\mathbf{k}}(\mathbf{z}, \mathbf{z}') = -\frac{i}{2} \sum_{\ell + \mathbf{m} = \mathbf{k}} \begin{pmatrix} u_{\mathbf{m}} \mathbf{m} \cdot \mathbf{u}'_{\ell} + u'_{\mathbf{m}} \mathbf{m} \cdot \mathbf{u}_{\ell} \\ h_{\mathbf{m}} \mathbf{k} \cdot \mathbf{u}'_{\ell} + h'_{\mathbf{m}} \mathbf{k} \cdot \mathbf{u}_{\ell} \end{pmatrix} \quad (7)$$

where \mathbf{z}' is a second coefficient vector with components $\mathbf{u}'_{\mathbf{k}}$ and $h'_{\mathbf{k}}$. \mathbf{A} denotes the infinite block-diagonal matrix made of components $\mathbf{A}_{\mathbf{k}}$ with corresponding ordering to fit to $\mathbf{z} = (\mathbf{z}_{\mathbf{k}})_{\mathbf{k} \in \mathbb{Z}^2}$. The expression for $\mathbf{N}_{\mathbf{k}}$ has been symmetrized, which is not necessary at this point, but makes it easy to separate the interactions between different modes as in (12) below.

The matrix $\mathbf{A}_{\mathbf{k}}$ has three eigenvalues $\omega_{\mathbf{k}}^0 = 0$ and $\omega_{\mathbf{k}}^{\pm} = \pm \sqrt{1 + \text{Bu} |\mathbf{k}|^2}$. Two of them, ω^{\pm} , correspond to inertia-gravity waves, henceforth referred to as *gravity waves* for short. The other one, ω^0 , corresponds to a vortical mode, sometimes also referred to as Rossby mode or Rossby wave (here, it is a zero-frequency “wave” since the f is constant.) In the more general case when f is slowly varying in space, the Rossby wave frequency is finite but remains much smaller than $|\omega^{\pm}|$ (see, e.g., Appendix B of Eden et al. 2019b for an expression using first-order perturbation theory).

The corresponding left and right eigenvectors, satisfying $(\mathbf{p}_{\mathbf{k}}^{\sigma})^{\text{H}} \mathbf{A}_{\mathbf{k}} = (\mathbf{p}_{\mathbf{k}}^{\sigma})^{\text{H}} \omega_{\mathbf{k}}^{\sigma}$ and $\mathbf{A}_{\mathbf{k}} \mathbf{q}_{\mathbf{k}}^{\sigma} = \omega_{\mathbf{k}}^{\sigma} \mathbf{q}_{\mathbf{k}}^{\sigma}$ for $\sigma = 0, -, +$ are (see, e.g., Eden et al., 2019b)

$$\mathbf{q}_{\mathbf{k}}^{\sigma} = \begin{pmatrix} \frac{\sigma |\omega| \mathbf{k} + i \mathbf{k}^{\perp}}{1 - \sigma^2 \omega^2} \\ 1 \end{pmatrix}, \quad \mathbf{p}_{\mathbf{k}}^{\sigma} = n_{\mathbf{k}}^{\sigma} \begin{pmatrix} \frac{\sigma |\omega| \mathbf{k} + i \mathbf{k}^{\perp}}{1 - \sigma^2 \omega^2} \\ \text{Bu}^{-1} \end{pmatrix} \quad (8)$$

178 with normalization

$$n_{\mathbf{k}}^\sigma = \frac{\text{Bu}}{1 + \sigma^2} \frac{|\sigma^2 \omega^2 - 1|}{1 + \text{Bu} |\mathbf{k}|^2} \quad (9)$$

179 so that orthonormality holds, i.e., $(\mathbf{p}_{\mathbf{k}}^\sigma)^\text{H} \mathbf{q}_{\mathbf{k}}^{\sigma'} = \delta_{\sigma, \sigma'}$. The superscript H denotes
 180 the Hermitian conjugate. We write \mathbb{P}^0 to denote the orthogonal projector onto
 181 the vortical modes, and \mathbb{P}^+ and \mathbb{P}^- to denote the orthogonal projector onto
 182 each of the gravity wave modes, given for every fixed wavenumber \mathbf{k} by

$$\mathbb{P}_{\mathbf{k}}^\sigma = \mathbf{q}_{\mathbf{k}}^\sigma (\mathbf{p}_{\mathbf{k}}^\sigma)^\text{H} \quad \text{for } \sigma = 0, -, +, \quad (10)$$

183 set $\mathbf{z}^\sigma = \mathbb{P}^\sigma \mathbf{z}$, $\mathbf{N}^\sigma = \mathbb{P}^\sigma \mathbf{N}$, and introduce the short-hand notation $\mathbb{P}^{\text{GW}} =$
 184 $\mathbb{P}^+ + \mathbb{P}^-$ and $\mathbf{z}^{\text{GW}} = \mathbf{z}^+ + \mathbf{z}^-$. In the basis of right eigenvectors, the linear part
 185 of the components of (5) is diagonal, so that

$$\frac{d\mathbf{z}_{\mathbf{k}}^\sigma}{dt} - i\omega_{\mathbf{k}}^\sigma \mathbf{z}_{\mathbf{k}}^\sigma = \text{Ro } \mathbf{N}_{\mathbf{k}}^\sigma(\mathbf{z}, \mathbf{z}), \quad (11)$$

where the case $\sigma = 0$ corresponds to the slow (vortical) modes and $\sigma = \pm$ to
 the fast (gravity wave) modes. We note that

$$\mathbf{N}^\sigma(\mathbf{z}, \mathbf{z}) = \mathbf{N}^\sigma(\mathbf{z}^0, \mathbf{z}^0) + 2\mathbf{N}^\sigma(\mathbf{z}^0, \mathbf{z}^{\text{GW}}) + \mathbf{N}^\sigma(\mathbf{z}^{\text{GW}}, \mathbf{z}^{\text{GW}}), \quad (12)$$

186 so that we can sort the nonlinear interactions into vortical-vortical, vortical-
 187 gravity, and gravity-gravity mode interactions. Due to this coupling, an accurate
 188 description of the slow manifold will involve not only the linear geostrophic
 189 modes \mathbf{z}^0 , but also some non-zero contributions in the linear gravity wave modes
 190 $\mathbf{z}^{\text{GW}} = \mathbf{z}^+ + \mathbf{z}^-$.

191 3 Nonlinear high-order balance

192 3.1 Higher order balance procedure

193 We assume a state in which the gravity waves are initially small, namely $\mathbf{z}^\pm =$
 194 $O(\text{Ro})$. Accordingly, we expand the gravity wave amplitudes as

$$\mathbf{z}^\pm = \text{Ro } \mathbf{z}_1^\pm + \text{Ro}^2 \mathbf{z}_2^\pm + \text{Ro}^3 \mathbf{z}_3^\pm + \dots \quad (13)$$

195 It can be shown that, under this assumption, the gravity wave amplitudes are
 196 growing only weakly in time, so that this ansatz remains consistent for an ex-
 197 tended period of (slow) time.

198 The time derivative in (5) includes fast gravity waves with frequency ω^\pm
 199 and the slow growth and decay of the amplitudes of both slow and fast modes
 200 due to the nonlinear interactions. Therefore, we introduce a slow time variable
 201 $s = \text{Ro } t$ so that $d/dt = \partial_t + \text{Ro } \partial_s$.

202 Assume now that \mathbf{z}^0 is a function of slow time only, whereas \mathbf{z}^\pm is a function
 203 of slow and fast times. Thus, (11) for the vortical mode $\sigma = 0$ reads

$$\text{Ro } \partial_s \mathbf{z}^0 = \text{Ro } \mathbf{N}^0(\mathbf{z}, \mathbf{z}). \quad (14)$$

Using (12) and inserting the expansion (13), we see that the leading order of (14) is given by

$$\partial_s z^0 = N^0(z^0, z^0). \quad (15)$$

This first order balanced model is identical to the familiar (first order) quasi-geostrophic approximation, as observed by Leith (1980). Only the vortical modes z^0 are involved, and this is why (15) – which is a spectral representation of the quasi-geostrophic potential vorticity equation – is closed.

To obtain a model which is second or higher order accurate, diagnostic relations for the *ageostrophic balanced modes* or *slaved modes* z_n^\pm need to be derived. These modes are part of the balanced motion since they evolve only slowly (Kafabad and Bartello, 2018; McIntyre and Norton, 2000; Warn et al., 1995). The lowest order of these, z_1^\pm , corresponds to the first order (ageostrophic) variables in the quasi-geostrophic approximation (Leith, 1980), which are not needed to predict the evolution of the geostrophic variables and generally unknown in the quasi-geostrophic model. However, they are required for all higher order balance models.

To first order in Ro, equation (5) for the gravity wave modes reads

$$\partial_t z_1^\pm - i\omega^\pm z_1^\pm = N^\pm(z^0, z^0), \quad (16)$$

where ω^\pm denotes the diagonal operator acting as multiplication by ω_k^+ or ω_k^- , respectively, on each of the eigenspaces.

A non-zero time derivative in (16) reflects the existence of fast waves with frequency ω^\pm . Thus, to enforce a balanced state, it is necessary to have

$$z_1^\pm = i N^\pm(z^0, z^0) / \omega^\pm. \quad (17)$$

Inserting this relation back into (5), we obtain a second order balance model of the form

$$\partial_s z^0 = N^0(z^0, z^0) + 2 \text{Ro} N^0(z^0, z_1^{\text{GW}}). \quad (18)$$

Setting $\partial_t z_n^\pm = 0$ to suppress generation of gravity waves in general, we write (11) as

$$\begin{aligned} \sum_{n=1}^{\infty} (\text{Ro}^{n+1} \partial_s - i\omega^\pm \text{Ro}^n) z_n^\pm &= \text{Ro} N^\pm(z^0, z^0) \\ &+ 2 \sum_{n=1}^{\infty} \text{Ro}^{n+1} N^\pm(z^0, z_n^{\text{GW}}) + \sum_{n=2}^{\infty} \text{Ro}^{n+1} \sum_{i+j=n} N^\pm(z_i^{\text{GW}}, z_j^{\text{GW}}) \end{aligned} \quad (19)$$

with $z_n^{\text{GW}} = z_n^+ + z_n^-$. In particular, the second, third, and fourth orders are given by

$$\partial_s z_1^\pm - i\omega^\pm z_1^\pm = 2 N^\pm(z^0, z_1^{\text{GW}}) \quad (20a)$$

$$\partial_s z_2^\pm - i\omega^\pm z_2^\pm = 2 N^\pm(z^0, z_2^{\text{GW}}) + N^\pm(z_1^{\text{GW}}, z_1^{\text{GW}}) \quad (20b)$$

$$\partial_s z_3^\pm - i\omega^\pm z_3^\pm = 2 N^\pm(z^0, z_3^{\text{GW}}) + 2 N^\pm(z_1^{\text{GW}}, z_2^{\text{GW}}). \quad (20c)$$

Hence, we can calculate \mathbf{z}_2^\pm from (20a), \mathbf{z}_3^\pm from (20b), and so on. The slow time derivative $\partial_s \mathbf{z}_1^\pm$ in (20a) is calculated analytically by taking the derivative of (17) and inserting (15) as outlined in Kafiabad and Bartello (2018) and Eden et al. (2019a, Section 2). $\partial_s \mathbf{z}_2^\pm$ and higher are calculated by integrating the model with (the inverse Fourier transform of) $\mathbf{z}_0 + \text{Ro} \mathbf{z}_1^{\text{GW}}$ as initial condition for a few time steps and taking a finite difference. Since only slow time derivatives ∂_s show up, the slaved modes (or ageostrophic balanced modes) $\mathbf{z}_n^{\text{GW}} = \mathbf{z}_n^+ + \mathbf{z}_n^-$ are only slowly evolving in time, just as the vortical mode. The combination of vortical mode amplitude \mathbf{z}^0 and \mathbf{z}_n^{GW} defines the balanced mode in spectral space, and inverse Fourier transform yields the balanced flow in physical space. In the following, we will denote the slaved modes by

$$B_n(\mathbf{z}^0) = \sum_{i=1}^n \text{Ro}^i \mathbf{z}_i^{\text{GW}} = \sum_{i=1}^n \text{Ro}^i (\mathbf{z}_i^+ + \mathbf{z}_i^-). \quad (21)$$

3.2 Optimal balance in primitive variables

Optimal balance in primitive variables, which are \mathbf{u} and h for the single layer model, was introduced by Masur and Oliver (2020). The method works by integrating the model over an interval $[0, T]$ of artificial time τ while gradually switching on the nonlinear interactions. Initially, at $\tau = 0$, the nonlinear interactions are switched off and an exact *linear* mode decomposition allows the complete removal of gravity waves. When the nonlinear interactions are fully switched on, at $\tau = T$, the system is in a state which is nearly optimally balanced with regard to an evolution of the shallow water model in physical time. The method is based on the principle that, so long as the change between linear and fully nonlinear time evolution is slow, i.e., comparable to the physical motion on the slow time scale, a state on a slow manifold will continue to evolve close to it as the system and hence the manifold undergoes a slow deformation. In particular, since the fast energy is identically zero at $\tau = 0$, it will remain zero to a good approximation at $\tau = T$.

Usually, we would want to compute the balanced state which corresponds to a known physical field, the “base point variable”, such as \mathbf{z}^0 in the setup above. In that case, we obtain a boundary value problem in time, where the “linear end” boundary condition at $\tau = 0$ encodes that no gravity waves are present, and the “nonlinear end” boundary condition at $\tau = T$ encodes that the prescribed value of the base point variable is met.

Optimal balance is implemented by multiplying all nonlinear terms with a smooth monotonic “ramp function” $\rho(\tau/T)$, where $\rho: [0, 1] \rightarrow [0, 1]$ with $\rho(0) = 0$ and $\rho(1) = 1$. Further, a sufficient number of derivatives of ρ need to vanish at the temporal end points; Gottwald et al. (2017) give a rigorous analysis of why this is so. In this study, we use as ramp function

$$\rho(\theta) = \frac{f(\theta)}{f(\theta) + f(1 - \theta)}, \quad f(\theta) = \exp(-1/\theta), \quad (22)$$

which was shown to yield asymptotically the best performance in Masur and

Oliver (2020). For the shallow water equations in the form (3), this corresponds to the following set of equations:

$$\partial_\tau \mathbf{u} + f \mathbf{u}^\perp + \nabla h = -\text{Ro} \rho(\tau/T) \mathbf{u} \cdot \nabla \mathbf{u}, \quad (23a)$$

$$\partial_\tau h + \text{Bu} \nabla \cdot \mathbf{u} = -\text{Ro} \rho(\tau/T) \nabla \cdot (h \mathbf{u}). \quad (23b)$$

At the linear end, in the notation set up in Section 2.2, the boundary condition

$$\mathbb{P}^{\text{GW}} \mathbf{z}(0) = 0, \quad (23c)$$

encodes that no linear gravity waves are present. At the nonlinear end, we use the condition

$$\mathbb{P}^0 \mathbf{z}(T) = \mathbf{z}_*^0 \quad (23d)$$

where \mathbf{z}_*^0 denotes the prescribed linear vortical mode component of the flow. This is equivalent to taking the linear potential vorticity of the nonlinear flow as the “base point” coordinate. Other base point coordinates, such as nonlinear potential vorticity or height, have been explored in Masur and Oliver (2020).

The output balanced state is then given by

$$\mathbf{z}_{\text{bal}}^{\text{GW}} = \mathbb{P}^{\text{GW}} \mathbf{z}(T) \equiv B_{\text{opt}}(\mathbf{z}_*^0). \quad (24)$$

As described in Masur and Oliver (2020), we solve the boundary value problem approximately using a backward-forward nudging process. At the final time $\tau = T$, we impose boundary condition (23d), leaving the complementary components $\mathbb{P}^{\text{GW}} \mathbf{z}(T)$ unchanged. We then integrate backward up until $\tau = 0$. At this initial time, we impose boundary condition (23c), leaving the complementary components $\mathbb{P}^0 \mathbf{z}(0)$ unchanged. To close the cycle, we integrate forward again up to $\tau = T$. This cycle is iterated until, at $\tau = T$, the difference between consecutive updates falls below a certain tolerance threshold. It can be shown that, under a suitable smallness assumption for the vortical number, the iterates converge to a function that solves (23) up to possibly a small remainder which is comparable to the (exponentially small) balancing residual of optimal balance itself (Masur, 2022; Masur et al., 2023).

4 Experimental setup

4.1 Numerical schemes

To solve the single layer model (3), we discretize the spatially periodic domain of length $L = 2\pi$ with 255 grid points in each direction, and use the following two numerical schemes. The first is a pseudo spectral scheme with rotationally symmetric truncation of 2/3 of the largest wavenumber to compute the Fourier transforms of the convolutions of nonlinear terms in physical space, and is also used by and further detailed in Masur and Oliver (2020). The spatial mesh is an A-grid. The other scheme uses finite differences on a standard C-grid and is identical, except for the time stepping scheme, to the one used by Eden

et al. (2019b), where the discretization of the nonlinear terms in the momentum equation follows the energy-conserving scheme by Sadourny (1975). The time-stepping scheme for both cases is the third-order Adam–Bashforth method. In the spectral model, we use a time step selection based on the code by Poulin (2016), and in the finite difference model we use a fixed time step $\Delta t = 0.002$, unless noted otherwise. In both cases, there is no other damping in the model by frictional or mixing terms.

Note that for the balancing procedure and the diagnostics of the imbalance, we use the eigenvectors \mathbf{p}_k^σ and \mathbf{q}_k^σ representative for the discrete equations of the C-grid as given in Eden et al. (2019b) for the finite difference model, and the analytical version of \mathbf{p}_k^σ and \mathbf{q}_k^σ given by (8) for the spectral model on the A-grid. We note that the use of eigenvectors that are compatible with the numerical scheme is crucial for the quality of balance.

4.2 Diagnosed imbalance

As we have no direct access to a well-balanced reference state, we evaluate the balancing schemes via the following notion of *diagnosed imbalance*. Any balance scheme can be seen a map from a “base point”, here the linear vortical mode contribution \mathbf{z}^0 , to the remaining phase space coordinates, here the linear gravity mode contribution \mathbf{z}^{GW} , which we express as

$$\mathbf{z}^{\text{GW}} = B(\mathbf{z}^0). \quad (25)$$

This map may be $B = B_n$, the higher order balance to order n described in Section 3.1, or $B = B_{\text{opt}}$, the result of the optimal balance procedure as described in Section 3.2. We perform the following steps:

- (i) Given a prescribed base point \mathbf{z}_*^0 , initialize the full nonlinear model at (physical) time $t = 0$ in a balanced state by setting $\mathbf{z}(0) = \mathbf{z}_*^0 + B(\mathbf{z}_*^0)$.
- (ii) Evolve this state by numerically solving the shallow water equations (5) starting from $t = 0$ up to some time $t = t'$. Set $\mathbf{z}' \equiv \mathbf{z}(t')$
- (iii) “Rebalance” the evolved flow, setting $\mathbf{z}'' = \mathbb{P}^0 \mathbf{z}' + B(\mathbb{P}^0 \mathbf{z}')$.
- (iv) Compute the *diagnosed imbalance* as the relative difference between the evolved state and the rebalanced state, i.e.,

$$I(\mathbf{u}) = \frac{\|\mathbf{u}' - \mathbf{u}''\|}{\frac{1}{2}(\|\mathbf{u}'\| + \|\mathbf{u}''\|)}, \quad (26)$$

and similarly for h , where $\|\cdot\|$ is the Euclidean norm (or root mean square) on the computational grid. We use separate norms for both \mathbf{u} and h since it is not obvious to define a single norm representative of the diagnosed imbalance that reflects the correct scaling behavior as $\text{Ro} \rightarrow 0$. In particular, the energy norm is not appropriate as our results, see Section 5, show that \mathbf{u} and h behave differently.

328 The diagnosed imbalance is based on the idea that the phase angles of the
 329 fast degrees of freedom are essentially random when viewed on the slow time
 330 scale. Therefore, it is highly unlikely that fast degrees of freedom, if present,
 331 will be preserved in the rebalancing step (iii) so that any fast component of
 332 the motion will, with high probability, contribute to the diagnosed imbalance.
 333 Numerical tests, e.g. as reported in von Storch et al. (2019) have shown that even
 334 in low-dimensional systems, the diagnosed imbalance provides a robust measure
 335 for the fast energy. Here, since the number of fast degrees of freedom is large, if
 336 the fast degrees of freedom were truly random and independently distributed, a
 337 central limit argument would prove that the variance of the diagnosed imbalance
 338 goes to zero as the number of degrees of freedom increases. This argument is
 339 not rigorous, of course, as there is no proof of statistical independence in some
 340 limiting regime.

341 However, it is possible that the diagnosed imbalance underestimates the level
 342 of fast energy because there might be recurrence points at which the actual fast
 343 dynamics has a close approach to the slow manifold given by the balance relation
 344 (25). But the diagnosed imbalance may also pick up the “real” fast wave signal
 345 due to spontaneous emission of gravity waves during the forward time evolution
 346 from $t = 0$ to $t = t'$. However, it appears that wave emission of balanced
 347 flow is in general very weak – only in case of instabilities of the flow significant
 348 wave generation can be detected (Chouksey et al., 2022). Consistent with this
 349 expectation, experiments with varying forward integration time t' support the
 350 conclusion that spontaneous emission does not contribute significantly to the
 351 results shown below.

352 Thus, even though not perfect, the diagnosed imbalance I is the most acces-
 353 sible and unbiased diagnostic tool to quantify the quality of balance obtained
 354 from a balance relation of the form (25).

355 4.3 Initialization

356 At time $t = 0$, we choose the base point coordinate for our balance comparison
 357 from two different flow configurations. The first configuration is taken from
 358 Masur and Oliver (2020) and constructed from a random height anomaly field
 359 h where the amplitude of the Fourier coefficients $h_{\mathbf{k}}$ are adjusted so that the
 360 spectral energy density $S(k)$ is given by

$$h_{\mathbf{k}} \sim r \sqrt{S(k)/k} \quad \text{with} \quad S(k) = \frac{k^7}{(k^2 + a k_0^2)^{2b}} \quad (27)$$

361 where $k = |\mathbf{k}|$ and r is a random complex number with zero mean and unit
 362 variance. With $b = (7 + d)/4$ and $a = (4/7)b - 1$, the spectral slope becomes
 363 $S(k) \sim k^{-d}$ as $k \rightarrow \infty$, with the maximum of $S(k)$ at $k = k_0$. We choose $d = 6$
 364 and $k_0 = 6$. The base point is then obtained by projecting $\mathbf{z} = (0, 0, h_{\mathbf{k}})$ onto
 365 the geostrophic mode, i.e., setting $\mathbf{z}_*^0 = \mathbb{P}_{\mathbf{k}}^0 \mathbf{z}$, then rescaling the result such that
 366 $\max|h| = 0.2$, which finally yields \mathbf{z}_{rand} .

367 Fig. 1 shows the resulting optimally balanced initial state $\mathbf{z}_{\text{rand}} + B_{\text{opt}}(\mathbf{z}_{\text{rand}})$
 368 for the spectral model with $\text{Ro} = 0.1$ (upper row), and the evolved state at

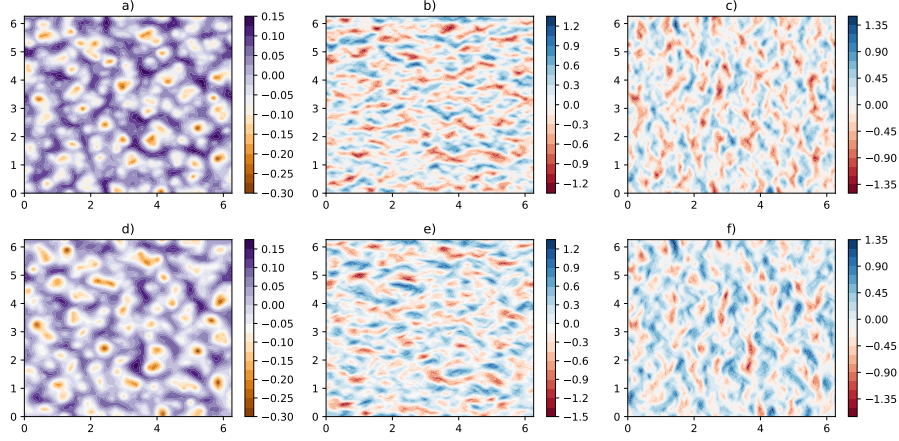


Figure 1: Random field initialization $\mathbf{z}_{\text{rand}} + B_{\text{opt}}(\mathbf{z}_{\text{rand}})$ in the spectral model for $\text{Ro} = 0.1$. We show h , u , and v at $t = 0$ in panels (a), (b), and (c), respectively, as well as the evolved state at $t' = 0.5/\text{Ro}$ (d-f). For the optimal balance method, the ramp time is $T = 2$ and the convergence threshold is 10^{-4} .

369 $t' = 0.5/\text{Ro}$ (lower row) from which the diagnosed imbalance is then computed
370 as laid out in Section 4.2. The evolved state is moderately different from the
371 state at $t = 0$. The corresponding fields for the finite difference model and
372 the different balancing methods are visually very similar, but the diagnosed
373 imbalance differs as discussed below. Further, the fields for \mathbf{z}_{rand} , which is
374 balanced only to zero order, are visually very close to $\mathbf{z}_{\text{rand}} + B_{\text{opt}}(\mathbf{z}_{\text{rand}})$, but
375 do contain a substantial contribution of fast motion.

376 The second configuration is a developing instability from two counter-flowing
377 jets in the double periodic domain, also used by Eden et al. (2019b), initially of
378 the form

$$u(y) \sim e^{-(y-L/4)^2/(L/50)^2} - e^{-(y-3L/4)^2/(L/50)^2} \quad (28)$$

379 where, as before, $L = 2\pi$ denotes the extent of the domain. We use the Fourier
380 transform of (28), $u_{\mathbf{k}}$, plus a small sinusoidal perturbation in the corresponding
381 $h_{\mathbf{k}}$ from $h \sim \sin(10\pi x/L)$ to form the state vector $\mathbf{z} = (u_{\mathbf{k}}, 0, h_{\mathbf{k}})$. The corre-
382 sponding sinusoidal perturbation in v is chosen to be about 10^{-5} times smaller
383 than the jet-like flow in u . As before, we obtain the base point by projecting
384 \mathbf{z} on the geostrophic mode, i.e., $\mathbf{z}_*^0 = \mathbb{P}_{\mathbf{k}}^0 \mathbf{z}$ (again, with the projector chosen to
385 be compatible with the numerical scheme in use). The amplitude of \mathbf{z}_*^0 is then
386 scaled to yield a maximum jet speed of $u = 1.4$, which finally yields \mathbf{z}_{jet} .

387 Fig. 2 (upper row) shows the resulting jet-like balanced initial condition
388 $\mathbf{z}_{\text{jet}} + B_4(\mathbf{z}_{\text{jet}})$ in the finite difference model for $\text{Ro} = 0.1$. Both models are
389 integrated from $t = 0$ to $t = t' = 4/\text{Ro}$ where the imbalance I is diagnosed.
390 Here, we choose a larger t' compared to the random field configuration to allow
391 the flow to fully develop its instability where it may emit waves. The fully

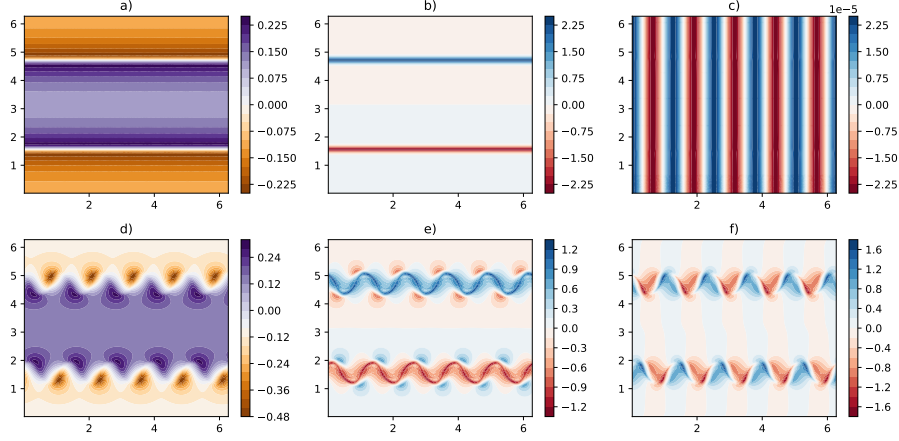


Figure 2: As Fig. 1, but for the jet flow initialization $\mathbf{z}_{\text{jet}} + B_4(\mathbf{z}_{\text{jet}})$ in the finite difference model for $Ro = 0.1$. We show the fields at $t = 0$ (upper row) and the evolved state at $t' = 4/Ro$ (lower row).

developed instability can be seen in Fig. 2 (lower row) for the finite difference model, the fields for the spectral model and using different balancing methods are again visually very similar.

5 Results

In this section, we discuss the performance of the two balancing methods – higher order (B_1, \dots, B_4) and optimal balance (B_{opt}) – in the two different models – the spectral (SPEC) and finite difference (DIFF) discretizations – using the two different balanced initial conditions – random (\mathbf{z}_{rand}) and jet-like (\mathbf{z}_{jet}). In general, the diagnosed imbalance or residual wave signal is very small in both models, for both initial conditions. We therefore detect no significant wave emission in any of the experiments discussed here in agreement with the results of Chouksey et al. (2022). However, we shall describe and discuss small differences in performance which are particularly visible in the jet-like test case.

5.1 Random initial conditions

Fig. 3 shows the diagnosed imbalance in DIFF for \mathbf{z}_{rand} using B_n for different orders n . The residual wave signal scales as expected for B_0 to B_2 , i.e. as Ro for B_0 , as Ro^2 for B_1 , and as Ro^3 for B_2 . For B_3 and B_4 , the expected scaling is only seen for small Rossby numbers. In fact, for Ro getting close to 1, the residuals start growing when the order is increased. It is difficult to judge if this behavior is due to actual gravity wave emission, imperfection of our implementation of the method, an already diverging power series, or numerical

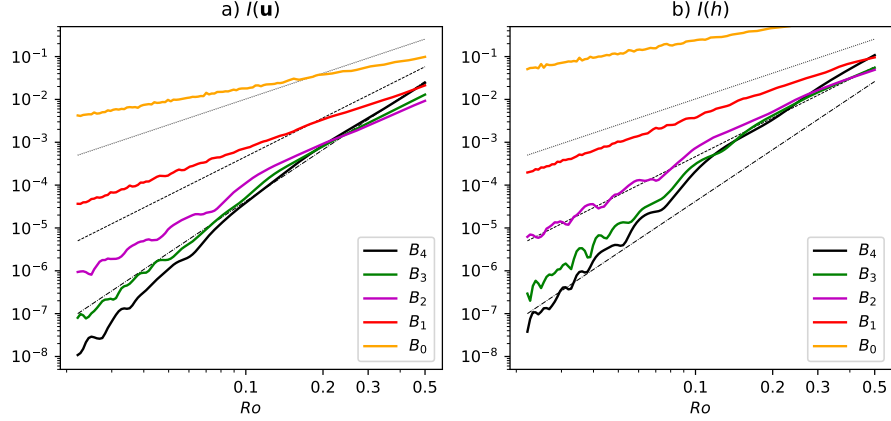


Figure 3: Diagnosed imbalance $I(u)$ (a) and $I(h)$ (b) in DIFF using the field z_{rand} balanced with B_4 (black), B_3 (green), B_2 (magenta), B_1 (red), and B_0 (orange), as a function of Rossby number Ro . The thin black lines denote different scaling laws, i.e. Ro^2 (dotted), Ro^3 (dashed), and Ro^4 (dashed-dotted).

truncation errors. We expect that for Ro approaching 1, the optimal truncation is of rather low order so that the quality of balance decreases when including higher orders terms, as seen in Fig. 3. However, we noticed that small details in the numerical coding affect the residual drastically (not shown), as already noted by Eden et al. (2019a), pointing towards a large role of numerical truncation errors.

Fig. 4 compares the performance of B_4 and B_{opt} in SPEC and DIFF. B_{opt} scales in general similar to B_4 in all cases, but the overall level of the residuals can be different, although still very small in all cases. The residual wave signal is here slightly larger in SPEC than DIFF. However, using also $T = 2$ for B_{opt} in DIFF, the residuals are getting very similar to B_{opt} in SPEC (not shown). The impact of ramp time T on the diagnosed imbalanced is documented in Masur and Oliver (2020) and not repeated here. For larger T , the residual gets smaller, but for even larger T , the residual increases again. The optimal T for this configuration is between $T = 2$ and $T = 4$ for DIFF, but for SPEC the optimal T is between $T = 0.5$ and $T = 2$. This points towards the importance of the numerics for the performance of the optimal balance method. Masur and Oliver (2020) also discussed the impact of the threshold to terminate the iteration in B_{opt} ; they show that the impact is minor and the same is true here. The impact of the choice of the ramp function $\rho(\tau/T)$ is also documented in Masur and Oliver (2020); here we use the exponential ramp function given in (22), which is the optimal choice in Masur and Oliver (2020).

The diagnosed imbalance for DIFF using B_{opt} with $T = 4$ gets rather noisy at small Ro and fluctuates by orders of magnitude for small changes in Ro . When

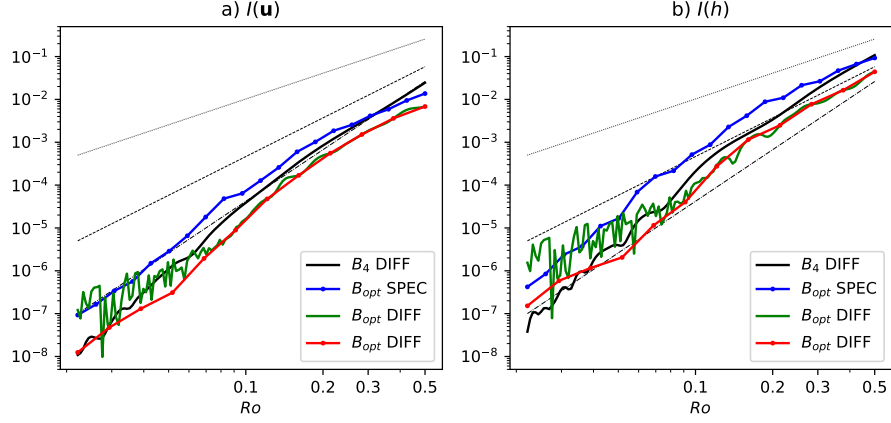


Figure 4: Diagnosed imbalance $I(\mathbf{u})$ (a) and $I(h)$ (b) using the field \mathbf{z}_{rand} balanced with B_4 in DIFF (black), B_{opt} in SPEC with $T = 2$ (blue), B_{opt} in DIFF with $T = 4$ (green), and B_{opt} in DIFF with $T = 4$ but 10 times smaller time step (red). The dotted lines denote different scaling laws, i.e. Ro^2 , Ro^3 , and Ro^4 . The thin black lines denote different scaling laws, i.e. Ro^2 (dotted), Ro^3 (dashed), and Ro^4 (dashed-dotted). Dots denote individual experiments.

437 decreasing the time step by a factor 10, this behavior disappears, the dependency
 438 of the diagnosed imbalance on Ro becomes smooth, and the residuals get again
 439 smaller than with larger time step. An accurate time stepping scheme appears
 440 therefore important for the performance of optimal balance, while this is not
 441 the case for B_4 (not shown). Reducing the time step further by an overall factor
 442 of 20 reduces the residual only at very small Ro (not shown), so that for the
 443 parameter range shown, the results for B_{opt} are not affected by the accuracy of
 444 the time stepping scheme and other errors appear to dominate.

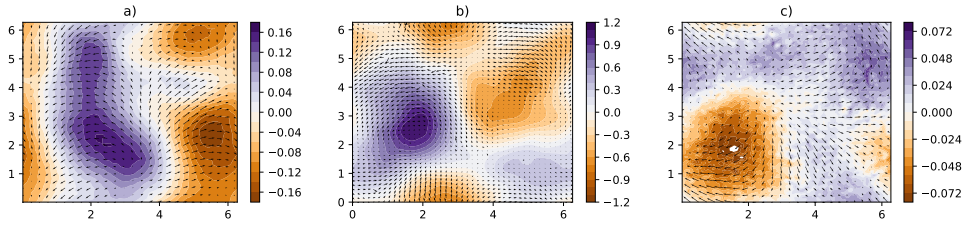


Figure 5: Residual wave signal $\mathbf{z}' - \mathbf{z}''$ after rebalancing at $t = 0.5/\text{Ro}$ for $\text{Ro} = 0.1$ and \mathbf{z}_{rand} in DIFF and B_4 (a), in SPEC and B_{opt} with $T = 2$ (b), and in DIFF and B_{opt} with $T = 4$ and 10 times smaller time step (c). We show h/Ro^4 in color and u, v as arrows, with magnitude of $O(10^{-6})$.

Fig. 5 shows the residual wave signal $\mathbf{z}' - \mathbf{z}''$ after rebalancing at $t = 0.5/\text{Ro}$ for a fixed Rossby number $\text{Ro} = 0.1$ using \mathbf{z}_{rand} , both models and balancing methods. For all cases, the residual shows in all variables a large-scale pattern, clearly deviating from geostrophic balance. We see no systematic difference for the different balancing methods in their spatial patterns, except for the different magnitude of the residual. However, the case using DIFF and B_{opt} with $T = 4$ and smaller time step shows also noise on smaller scales which is not present for the other cases which have larger diagnosed imbalance. Using a time step 20 times smaller, the noise remains the same, and also the diagnosed imbalance as mentioned before.

5.2 Jet-like initial conditions

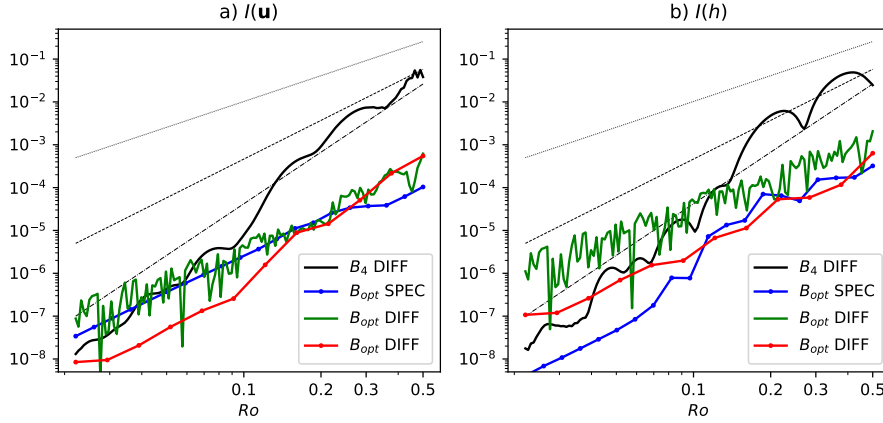


Figure 6: Diagnosed imbalance $I(\mathbf{u})$ (a) and $I(h)$ (b) for \mathbf{z}_{jet} in DIFF balanced with B_4 (black), in SPEC using B_{opt} with $T = 4$ (blue), in DIFF using B_{opt} with $T = 4$ (green), and in DIFF using B_{opt} with $T = 4$ but 20 times smaller time step (red). The thin black lines denote different scaling laws, i.e. Ro^2 (dotted), Ro^3 (dashed), and Ro^4 (dashed-dotted). Dots denote individual experiments.

Fig. 6 shows the diagnosed imbalance of both methods in both models using the jet-like initial conditions instead of the random case. B_4 scales roughly as Ro^4 , similar to the case using \mathbf{z}_{rand} , pointing again to numerical truncation errors for the highest orders. B_{opt} scales shallower, but shows smaller residuals for $\text{Ro} > 0.1$ than B_4 . B_{opt} in DIFF depends again on the quality of the time stepping method, i.e. the fluctuations of the diagnosed imbalance for only small changes in Ro seen at small $\text{Ro} < 0.1$ for the normal time step disappear using a 20 times smaller time step. B_{opt} in SPEC has smaller residuals than B_{opt} in DIFF for $\text{Ro} < 0.1$ in $I(h)$, but larger residuals than B_{opt} in DIFF for $\text{Ro} < 0.1$ in $I(\mathbf{u})$, while they are similar for $\text{Ro} > 0.1$. This shows that at the level of the very small residuals, the different model codes can better reduce the residuals

in different variables, and points again to the large role of numerical details and different errors for the quality of the balancing methods.

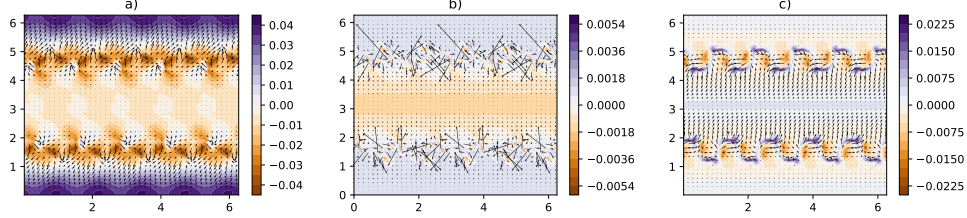


Figure 7: Residual wave signal $z' - z''$ after rebalancing at $t = 4/\text{Ro}$ for $\text{Ro} = 0.1$ in DIFF for z_{jet} using B_4 (a), in SPEC using B_{opt} with $T = 4$ (b), and in DIFF using B_{opt} with $T = 4$ and 20 times smaller time step (c). We show h/Ro^4 in color and u, v as arrows, with magnitude of $O(10^{-7})$.

Fig. 7 shows the residual wave signal for $\text{Ro} = 0.1$ for the different balancing methods and numerical models using z_{jet} . While the residuals in DIFF are on the same scale as the jet, the very small residual in h using B_{opt} in SPEC begins to show smaller scales similar to what has been reported before as gravity wave emission during frontogenesis (e.g. Plougonven and Snyder, 2007). However, note the small magnitude of the signal, which is much different to the wave signal reported in the previous section for the random field case.

5.3 Cross-balancing

In this section we discuss experiments where the imbalance $I(\mathbf{u})$ and $I(h)$ of the balanced state from the one method is diagnosed with the other method, which we refer to as cross-balancing. Note that using any balanced state from SPEC in DIFF or vice versa introduces errors already at zero order in Ro , because of the incompatible eigenvectors for the different numerical grids (A-grid vs. C-grid). Fig. 8 (green line) shows such a case, where the analytical eigenvectors $\mathbf{q}_k^\sigma, \mathbf{p}_k^\sigma$ appropriate for an A-grid instead of the corresponding ones for the C-grid are used for balancing with B_4 . The error is large and does not change much for smaller Ro . The spectral model behaves correspondingly. However, cross-balancing in the same numerical model with the same grid will provide additional information how the different (approximately) balanced states differ.

First, we balance DIFF using z_{rand} at $t = 0$ with B_4 , then we integrate to $t = 0.5/\text{Ro}$ and rebalance with B_{opt} (using $T = 4$) and diagnose the imbalance from the difference to the state at $t = 0.5/\text{Ro}$ (shown as yellow line in Fig. 8). Second, we initially balance with B_{opt} (using $T = 4$) and rebalance later with B_4 and diagnose the imbalance (shown as red line in Fig. 8). In both cases, the resulting diagnosed imbalance is only slightly larger than or almost equal to the maximum of $I(\mathbf{u})$ or $I(h)$ of the corresponding experiments using either B_{opt} or B_4 only. Thus, we conclude that both methods find a similar (approximately)

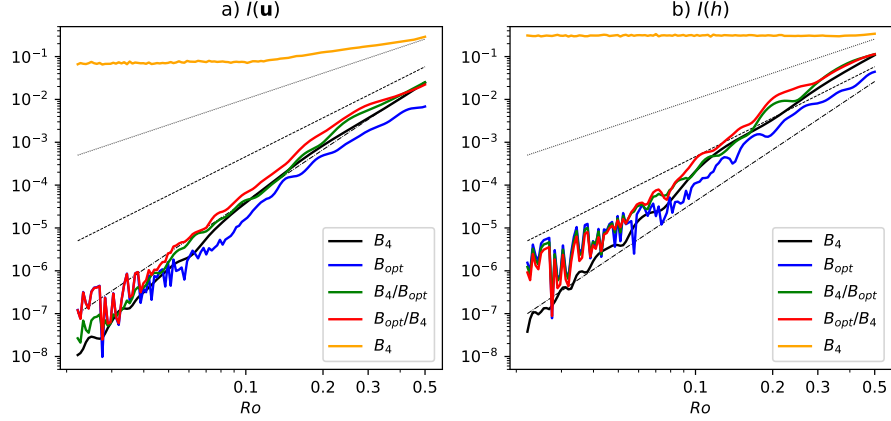


Figure 8: Diagnosed imbalance $I(\mathbf{u})$ (a) and $I(h)$ (b) for \mathbf{z}_{rand} in DIFF using B_4 (black), B_{opt} with $T = 4$ (blue), and the cross-balancing experiments using first B_4 then B_{opt} (green) and first B_{opt} then B_4 (red). The thin black lines denote different scaling laws, i.e. Ro^2 (dotted), Ro^3 (dashed), and Ro^4 (dashed-dotted). Also shown is a case with B_4 in DIFF (orange), where the eigenvectors for the A-grid are used instead of the correct ones.

balanced state.

6 Discussion and Conclusions

In this study, we compare two different methods to approximately balance geophysical flows: the higher order asymptotic implementation inspired by Warn et al. (1995) and the optimal balance implementation of Masur and Oliver (2020). We use here a single-layer shallow water model as example, but both methods can also readily be applied in three-dimensional models. We show that both methods can be understood as adding to the linear geostrophic mode \mathbf{z}_0 contributions $B_n(\mathbf{z}_0)$ and $B_{opt}(\mathbf{z}_0)$, respectively, taken from the linear wave modes, the so-called slaved modes, to generate a balanced state which evolves only slowly in time in the nonlinear model.

The main finding of this paper is that optimal balance and fourth-order in Rossby-number asymptotics can be considered equivalent for practical purposes. The residual wave signals of both balancing methods are comparable and show similar spatial patterns. There are, however, differences in the magnitude of the diagnosed imbalance for different model codes and initial conditions. It is difficult to decide if these differences are due to numerical issues such as truncation error or errors introduced by the time stepping scheme, or systematic. Cross-balancing, i.e. balancing the model with one method and diagnosing the imbalance with the other one, suggests that both methods find approximately

516 the same balanced states.

517 It has long been known that the quality of preservation of balance might
518 depend on the numerical scheme (see, e.g., Mohebalhojeh and Dritschel, 2000).
519 Here, we are able to show that adapting the notion of balance when changing
520 between the finite difference and the spectral scheme yields comparably very
521 good preservation of balance. It is only when mixing notions of balance across
522 schemes that quality of preservation of balance drops. For more practical ap-
523 plications, such as defining balance for observational data, this implies that
524 for a single-time snapshot of observational data the leading order balance is as
525 good (or bad) as higher-order balance. To increase the accuracy for the split-
526 ting of observational data into balance and imbalanced motion, the only way is
527 to use temporal-spatial data with a data assimilation scheme which includes a
528 higher-order characterization of balance that matches the numerical model.

529 A practical difference between the balancing methods presented here is the
530 computing resource demand. While the higher order balance method only needs
531 to run the model for a few time steps at maximum, followed by a few (fast)
532 Fourier transforms, the optimal balance method needs to integrate the model
533 over a sufficiently long ramping time, which needs significantly more computing
534 resources. On the other hand, the optimal balance model appears easier to
535 implement for a given numerical code.

536 Our results are presented in terms of the “diagnosed imbalance” which picks
537 up contributions that could be either due to imperfections of the balancing
538 method or due to actual wave emission of the balanced flow. We find that
539 the diagnosed imbalance, thus both contributing signals, decay rapidly with de-
540 creasing Rossby number. This implies, in particular that spontaneous emission
541 of gravity waves is negligible in flows within typical geophysical parameters,
542 in agreement with much earlier work such as Dritschel and Viúdez (2007) or
543 Chouksey et al. (2022) who found significant wave emission during balanced
544 shear flow instabilities in a three-dimensional flow only if symmetric or convec-
545 tive instabilities occur and the Rossby number is close to unity. This conclusion
546 is of practical relevance since several studies have previously reported signifi-
547 cant spontaneous wave emission by balanced flow (e.g. Borchert et al., 2014;
548 Plougonven and Snyder, 2007), which is also proposed as a significant sink of
549 meso-scale eddy energy in the ocean based on global estimates from labora-
550 tory experiments (Williams et al., 2008) and idealized numerical simulations
551 (Brüggemann and Eden, 2015; Sugimoto and Plougonven, 2016). It is possible
552 that the signals in those experiments are dominated by slaved modes rather
553 than actual wave emission, which calls to re-evaluate the experiments with the
554 high-order methods available now. It is, however, outside of the scope of the
555 present study to answer this issue.

556 There are two more obvious questions that also lie outside of the scope
557 of this paper. First, none of our results is directly applicable to the original
558 OPV formulation of Viúdez and Dritschel (2004) and it would be interesting
559 to benchmark their scheme in comparison with others. However, this raises a
560 new dimension of issues because, for a given resolution of the Eulerian grid,
561 the effective resolution of contour-advective semi-Lagrangian (CASL) scheme

used in OPV balance is much higher, and so is the computational cost. Thus, we choose to focus on balancing schemes that appear best suited for future application to operational implementations of full atmosphere and ocean models.

Second, our current model setting is highly idealized. Other studies have explored more complex settings for wave-vortex decomposition, such as McIntyre and Norton (2000) using potential vorticity inversion, Mohebalhojeh and Dritschel (2000) and Mirzaei et al. (2012) using the CASL and diabatic-CASL schemes respectively, and Chouksey et al. (2018), Eden et al. (2019a) and Chouksey et al. (2022) extending first order (Machenhauer, 1977) to higher order balance of Warn et al. (1995) for a range of flow regimes. We conjecture that both methods analyzed here are good candidates for computing high-accuracy balance in these and other circumstances. However, one common obstacle is that a spectral transform is necessary to project on the linear geostrophic mode, which is difficult to implement in nontrivial cases. We are currently working to resolve this issue, with the goal to apply the optimal balance method to realistic ocean models which will offer a variety of interesting practical applications of the method.

Acknowledgments

We thank the referees for their extremely detailed and constructive reviews which helped to considerably improve the manuscript. This paper is a contribution to subprojects W2, L2, and W6 of the Collaborative Research Centre TRR 181 “Energy Transfers in Atmosphere and Ocean” funded by the Deutsche Forschungsgemeinschaft (DFG, German Research Foundation) under project number 274762653. GTM is also supported through the Collaborative Research Center TRR 301 “The Tropopause Region in a Changing Atmosphere” funded by DFG under project number 428312742.

Declaration of Interests

The authors report no conflict of interest.

References

- Baer, F. and Tribbia, J. J. (1977). On complete filtering of gravity modes through nonlinear initialization. *Mon. Wea. Rev.*, 105(12):1536–1539.
- Borchert, S., Achatz, U., and Fruman, M. D. (2014). Gravity wave emission in an atmosphere-like configuration of the differentially heated rotating annulus experiment. *J. Fluid Mech.*, 758:287–311.
- Brüggemann, N. and Eden, C. (2015). Routes to dissipation under different dynamical conditions. *J. Phys. Oceanogr.*, 45(8):2149–2168.

Chouksey, M., Eden, C., and Brüggemann, N. (2018). Internal gravity wave emission in different dynamical regimes. *Journal of Physical Oceanography*, 48(8):1709–1730.

Chouksey, M., Eden, C., and Olbers, D. (2022). Gravity wave generation in balanced sheared flow revisited. *J. Phys. Oceanogr.*, 52(7):1351–1362.

Cotter, C. (2013). Data assimilation on the exponentially accurate slow manifold. *Phil. Trans. R. Soc. A*, 371(1991):20120300.

Dritschel, D. G. and Viúdez, Á. (2007). The persistence of balance in geophysical flows. *Journal of Fluid Mechanics*, 570:365–383.

Eden, C., Chouksey, M., and Olbers, D. (2019a). Gravity wave emission by shear instability. *J. Phys. Oceanogr.*, 49(9):2393–2406.

Eden, C., Chouksey, M., and Olbers, D. (2019b). Mixed rossby–gravity wave–wave interactions. *Journal of Physical Oceanography*, 49(1):291–308.

Gottwald, G. A., Mohamad, H., and Oliver, M. (2017). Optimal balance via adiabatic invariance of approximate slow manifolds. *Multiscale Model. Simul.*, 15(4):1404–1422.

Kafiabad, H. A. and Bartello, P. (2018). Spontaneous imbalance in the non-hydrostatic Boussinesq equations. *J. Fluid Mech.*, 847:614–643.

Leith, C. E. (1980). Nonlinear normal mode initialization and quasi-geostrophic theory. *J. Atmos. Sci.*, 37(5):958–968.

Lynch, P. (2006). *The Emergence of Numerical Weather Prediction: Richardson’s Dream*. Cambridge University Press.

Machenhauer, B. (1977). On the dynamics of gravity oscillations in a shallow water model with applications to normal mode initialization. *Beitr. Phys. Atmos.*, 50:253–271.

MacKay, R. S. (2004). Slow manifolds. In Dauxois, T., Litvak-Hinenzon, A., MacKay, R. S., and Spanoudaki, A., editors, *Energy Localisation and Transfer*, pages 149–192. World Scientific, Singapore.

Masur, G. T. (2022). *A numerical investigation of optimal balance for rotating shallow water flow*. Phd thesis, Jacobs University.

Masur, G. T., Mohamad, H., and Oliver, M. (2023). Quasi-convergence of an implementation of optimal balance by backward-forward nudging. *Multiscale Model. Simul.*, page to appear.

Masur, G. T. and Oliver, M. (2020). Optimal balance for rotating shallow water in primitive variables. *Geophys. Astrophys. Fluid Dyn.*, 114(4-5):429–452.

McIntyre, M. E. and Norton, W. A. (2000). Potential vorticity inversion on a hemisphere. *J. Atmos. Sci.*, 57(9):1214–1235.

Mirzaei, M., Mohebalhojeh, A. R., and Ahmadi-Givi, F. (2012). On imbalance generated by vortical flows in a two-layer spherical Boussinesq primitive equation model. *J. Atmos. Sci.*, 69(9):2819–2834.

Mohebalhojeh, A. R. and Dritschel, D. G. (2000). On the representation of gravity waves in numerical models of the shallow-water equations. *Q. J. Roy. Meteorol. Soc.*, 126(563):669–688.

Plougonven, R. and Snyder, C. (2007). Inertia–gravity waves spontaneously generated by jets and fronts. Part I: Different baroclinic life cycles. *J. Atmos. Sci.*, 64(7):2502–2520.

- 644 Poulin, F. J. (2016). PyRsw: Python rotating shallow water model. GitHub
645 repository, GitHub, commit c504456, <https://github.com/PyRsw/PyRsw>.
- 646 Sadourny, R. (1975). The dynamics of finite-difference models of the shallow-
647 water equations. *J. Atmos. Sci.*, 32(4):680–689.
- 648 Sugimoto, N. and Plougonven, R. (2016). Generation and backreaction of
649 spontaneously emitted inertia-gravity waves. *Geophys. Res. Letters*,
650 43(7):3519–3525.
- 651 Vanneste, J. (2013). Balance and spontaneous wave generation in geophysical
652 flows. *Ann. Rev. Fluid Mech.*, 45(1):147–172.
- 653 Vanneste, J. and Yavneh, I. (2004). Exponentially small inertia-gravity waves
654 and the breakdown of quasigeostrophic balance. *J. Atmos. Sci.*, 61(2):211–
655 223.
- 656 Viúdez, A. and Dritschel, D. G. (2004). Optimal potential vorticity balance of
657 geophysical flows. *J. Fluid Mech.*, 521:343–352.
- 658 von Storch, J.-S., Badin, G., and Oliver, M. (2019). The interior energy pathway:
659 inertial gravity wave emission by oceanic flows. In Eden, C. and Iske,
660 A., editors, *Energy Transfers in Atmosphere and Ocean*, pages 53–85.
661 Springer, Cham.
- 662 Warn, T., Bokhove, O., Shepherd, T., and Vallis, G. (1995). Rossby number
663 expansions, slaving principles, and balance dynamics. *Quart. J. Royal
664 Met. Soc.*, 121(523):723–739.
- 665 Williams, P. D., Haine, T. W., and Read, P. L. (2008). Inertia-gravity waves
666 emitted from balanced flow: Observations, properties, and consequences.
667 *J. Atmos. Sci.*, 65(11):3543–3556.